phys. stat. sol. (b) **245**, No. 7, 1356–1368 (2008) / **DOI** 10.1002/pssb.200844052

physica status solidi b
www.pss-b.com
basic solid state physics

Feature Article

Characterization of defects in silicon carbide by Raman spectroscopy

M. Hundhausen*, **R. Püsche, J. Röhrl, and L. Ley**

Lehrstuhl für Technische Physik, Institut für Physik der Kondensierten Materie, Universität Erlangen-Nürnberg, Erwin-Rommel-Straße 1, 91058 Erlangen, Germany

Received 30 January 2008, revised 19 March 2008, accepted 7 April 2008
Published online 3 June 2008

PACS 63.20.–e, 78.30.Hv, 78.30.Na, 81.05.Uw

* Corresponding author: e-mail martin.hundhausen@physik.uni-erlangen.de, Phone: +49 9131 852 7259, Fax: +49 9131 852 7889

We demonstrate the application of Raman spectroscopy as an optical non-contact method for the characterization of silicon carbide (SiC). The Raman spectra provide information about the polytype and thus can give direct information about microscopic inclusions of hexagonal polytypes in 3C-SiC grown by chemical vapor deposition (CVD) after annealing at elevated temperatures. Polytype conversion sets in at a about 1700 °C and at higher temperatures eventually results in larger domains of 6H-SiC where twin boundaries act as barriers against a complete polytype conversion. We study shallow donor states of phosphorus- and nitrogen-doped SiC using low temperature electronic Raman spectroscopy. The various low frequency transitions observed in nitrogen doped SiC are assigned to the valley-orbit transitions of electrons in the 1s-ground states of donors that occupy inequivalent lattice sites. During vacuum annealing at elevated temperature graphitization of the SiC surface occurs. Raman spectroscopy is used to verify that under well controlled conditions a monoatomic graphene layer exists. We observe a phonon hardening of that layer compared to free standing graphene that we ascribe mainly to strain induced by different thermal expansion coefficients of graphite and SiC.

1 Introduction In this contribution we review the application of Raman spectroscopy for the material characterization of SiC. Raman spectroscopy as an optical method is well suited as a non-contact analysis tool that requires little or no sample preparation. When employed in the form of micro Raman spectroscopy with a spatial resolution of 1–2 μm mapping of structural and electronic properties of SiC wafers by Raman spectroscopy is feasible.

Here we present three exemplary case studies. (i) The detection and quantification of polytype inclusions during the growth of cubic 3C-SiC; (ii) the assessment of the electronic levels of N and P co-doped 6H-, 4H-, and 15R-SiC; and (iii) the analysis of layer thicknesses and strain in few layer graphene grown on the Si-face of 6H-SiC. Whereas (i) and (iii) rely on the ability of Raman spectroscopy to measure phonon frequencies with high precision, case (ii) utilizes Raman scattering by electronic excitations, a mode of Raman scattering that is not as widely used as scattering by phonons but equally useful as we shall show.

2 Experimental setup The Raman spectrometer employed for these investigations was designed for high stray-light suppression even close to the laser line. We used a triple spectrometer (T64000 of Jobin–Yvon) equipped with 2400 lines/mm-gratings to achieve that goal. For detection a LN_2-cooled CCD detector was used whereas for excitation a HeNe-laser ($\lambda = 632$ nm) and a frequency doubled $NdYVO_4$-laser ($\lambda = 532$ nm) were employed. A confocal microscope served to focus the laser light on the sample and collect the scattered light to the entrance slit of the spectrometer. In this way a lateral resolution of 1–2 micron was obtained. By using a long distance objective lens samples could be measured when mounted in a liquid He-cryostat.

3 Polytype conversion in 3C-SiC grown by chemical vapor deposition SiC-devices are realized almost exclusively using hexagonal 6H- and 4H-SiC polytypes, for which wafers are commercially available

with up to 100 mm diameter and high crystal quality. This is not so for 3C-SiC which crystallises in the cubic zinc-blende structure. It has the smallest band gap (2.3 eV) and a high and isotropic mobility [1, 2]. However, there are no seed crystals available for the growth of large single crystals by vapor transport methods as there are for 6H- and 4H-SiC. Thus, 3C-SiC is exclusively grown as hetero-epitaxial layers by chemical vapor deposition (CVD) on silicon (100) substrates. The large lattice mismatch of 20% and an 8% difference in thermal expansion coefficient between 3C-SiC and Si leads invariably to 3C-SiC layers of poor quality with high concentrations of misfit dislocations, twins, stacking faults, and threading dislocations. Attempts to improve on this situation rely mostly on structured Si substrates. Thereby, hetero-epitaxy is initially limited to selected areas followed by lateral overgrowth [3, 4]. In one of these approaches, Nagasawa et al. grew 3C-SiC hetero-epitaxially on so-called "undulant" Si(100) surfaces by low pressure Chemical Vapor Deposition (CVD) [5]. The undulation consists of ridges and valleys running along $[\bar{1}10]$ and this results in 3C-SiC hetero-epitaxial layers in which the number of planar defects (twinning planes) is reduced in proportion to the thickness of the 3C-SiC layer [6, 7].

In this section, we review investigations on the relationship between the phase purity of 3C-SiC crystals grown by the "undulant-substrate"-technique and annealing steps at temperatures up to 2100 °C. To do so, we combine optical microscopy with spatially resolved micro Raman spectroscopy. Optical microscopy gives a first indication of phase heterogeneity of the crystal through a colour contrast that is related to different optical gaps for different SiC polytypes. Micro Raman spectroscopy with a lateral resolution of about 2 μm allows an unambiguous identification of the crystal phase of the inclusions and gives further information about strain in the crystal and substrate through its effect on line position and line shape. Successful physical vapor transport growth (PVT) of 3C-SiC by the modified Lely method on these 3C-SiC CVD substrates has been reported recently [8]. Hence, we extend our work to the phase purity of such PVT-samples and show how the polytype composition is affected by the phase transformation in the seed crystals that occur at growth temperature.

3.1 Experimental details The samples investigated were grown heteroepitaxially with the CVD-technique by Hoya-corporation on silicon substrates as described above. The thickness of the crystalline layers was ~200 μm after removal of the Si substrate. Crystal slices were cut and polished with surfaces parallel to the (110) and the $(\bar{1}10)$ crystallographic planes of 3C-SiC, respectively. We shall refer to them as (110) and $(\bar{1}10)$ cross sections in the following. These slices were subsequently annealed for 30 min in an argon atmosphere at temperatures between 1700 °C and 2100 °C. For the annealing, the samples were mounted on small SiC spacers to avoid direct contact of the samples with the graphite susceptor that was used as a support in the annealing oven. The sample temperature was measured with a pyrometer. A second set of samples was used as seed crystals in physical vapor transport (PVT) growth in an attempt to grow bulk 3C-SiC crystals ~500 μm thick. The growth was performed at a temperature of about 1900 °C. From these PVT-crystals similar (110) and $(\bar{1}10)$-oriented slices were produced in order to check if 3C-SiC crystals of sufficient phase purity had grown.

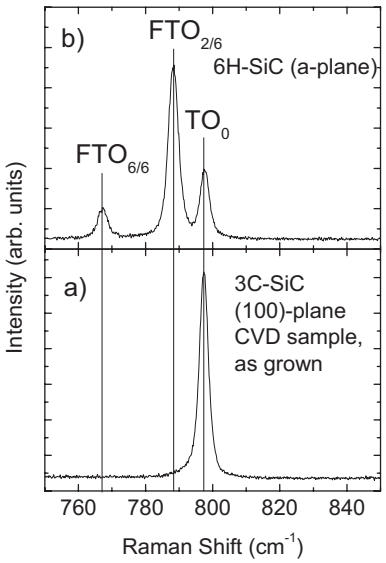

Figure 1 Reference spectra of a) pure 3C-SiC ((100)-plane) and b) pure 6H-SiC (*a*-plane). Note that the TO_0 mode is present in both spectra, though with a slight difference in frequency of the order of 1 cm^{-1}.

A first investigation of all crystal slices was performed by an optical microscope in the dark field mode where different polytypes appear in different colour. Unpolarised Raman spectra in the energy range from 720 cm^{-1} to 850 cm^{-1} were then recorded at 2 μm-spots that were selected from the microscopic images. As demonstrated in Fig. 1a 3C-SiC has only one phonon mode in that energy range, namely the zone center transversal optical phonon mode TO_0 at 796 cm^{-1}. For 6H-SiC (Fig. 1b) two additional folded phonon modes are observed, the $FTO_{6/6}$ at 767 cm^{-1} and the most intense $FTO_{2/6}$ mode at 789 cm^{-1} [9] which have been used to identify 6H-SiC inclusions in 3C-SiC. Because Raman intensities depend on the scattering geometry and hence the crystal orientation which is not known a priori, it is difficult to quantify the 6H-SiC content. Nevertheless, Raman measurements are a very sensitive method to detect even small polytype inclusions in the 3C-SiC host crystal.

3.2 Results In order to investigate the temperature induced polytype conversion in the seed crystal, we undertook a systematic annealing study of 3C-SiC CVD samples grown on undulant Si substrates after removal of the Si substrate [5]. The annealing was performed as explained

above. After annealing, (110) cross sections were prepared. We emphasize that all samples were purely 3C-SiC before any annealing took place. In the following we discuss two temperature regimes separately. At 1800 °C and above, we always observe the spectra of both the 3C-SiC and 6H-SiC polytypes. The frequencies of the phonon modes agree with those of the reference spectra in Fig. 1. After annealing at 1700 °C parts of the sample exhibit again three mode spectra, however, with one mode frequency deviating significantly from the reference $FTO_{2/6}$ frequency of 6H-SiC. We discuss the different temperature regimes in the following subsections separately.

3.2.1 Annealing temperature at and above 1800 °C Figure 2 shows typical microscopic images of the (110) cross sections of annealed CVD samples. The annealing temperature increases from 1800 °C for the bottom image to 2100 °C for the top image. The lower boundary of each image coincides with the original Si–SiC interface, i.e. with the beginning of the CVD growth on the undulant Si substrate. In contrast to as-grown CVD crystals, which show homogeneously coloured images, the annealed samples exhibit regions with different contrast and well defined borders parallel to the $(\bar{1}11)$ or $(1\,\bar{1}1)$ planes of the cubic crystal. Some of these borders are highlighted by white lines in Fig. 2. The differently coloured inclusions start from the top of the crystals and extend downwards no further than a position that is indicated by the dashed lines in Fig. 2. Note that this borderline moves closer to the Si–SiC interface with increasing annealing temperature without ever reaching it. The crosses on the images indicate some of the positions on the samples where Raman spectra were taken. Marks denoted with A are centred in a translucent region of the crystals, marks labelled B are at the interface region mentioned above and cross marks labelled with C are positioned outside of the translucent portions of the crystals well away from the interfacial region. The corresponding Raman spectra prove that the spots labelled A are converted to 6H-SiC, whereas the spectra outside of the transparent regions (spot C) still consist mainly of 3C-SiC as demonstrated in Fig. 2 for the sample annealed at 1900 °C.

The spectra taken in the interfacial region (B) are almost pure 3C-SiC for annealing temperatures at and below 2000 °C. After annealing at 2100 °C the interfacial region does begin to convert to 6H-SiC as well. However, starting from the former Si–SiC interface, a 20 μm thick region, extending laterally over the whole crystal, remains where the 6H-SiC content is much smaller than in the upper region of the crystal. The borderline is indicated by the dotted line in Fig. 2. There is no indication of polytypes other than 3C-SiC and 6H-SiC for annealing temperatures between 1800 °C and 2100 °C.

3.2.2 Annealing at 1700 °C The sample annealed at 1700 °C exhibits different features in the Raman spectra compared to samples annealed at higher temperatures, while the microscopic image of the cross section (Fig. 3) is similar to the samples annealed at higher temperatures.

We again find converted regions with different colour that start at the top of the CVD-layer of the crystal. These inclusions, however, do not reach as far to the bottom as they do for the higher annealing temperatures; rather they terminate roughly in the middle of the crystal. Again, the translucent regions are sharply separated from the yellowish regions with borders parallel to the $(\bar{1}11)$ or $(1\,\bar{1}1)$

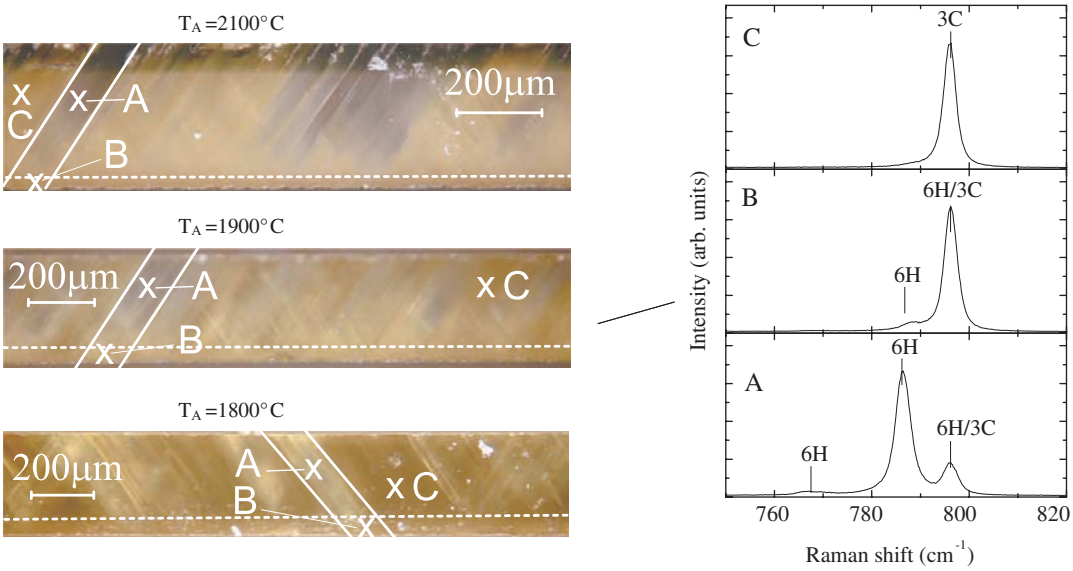

Figure 2 (online colour at: www.pss-b.com) Left: Typical microscopic images of (110) cross sections of a 3C-SiC CVD-sample grown on undulant Si(100). The samples are about 200 μm thick and annealed at temperatures increasing from 1800 °C (bottom) to 2100 °C (top). Right: Raman spectra recorded at points A, B, and C as indicated in the corresponding microscopic image of the sample annealed at 1900 °C. The spectra are representative for the corresponding points in the other samples.

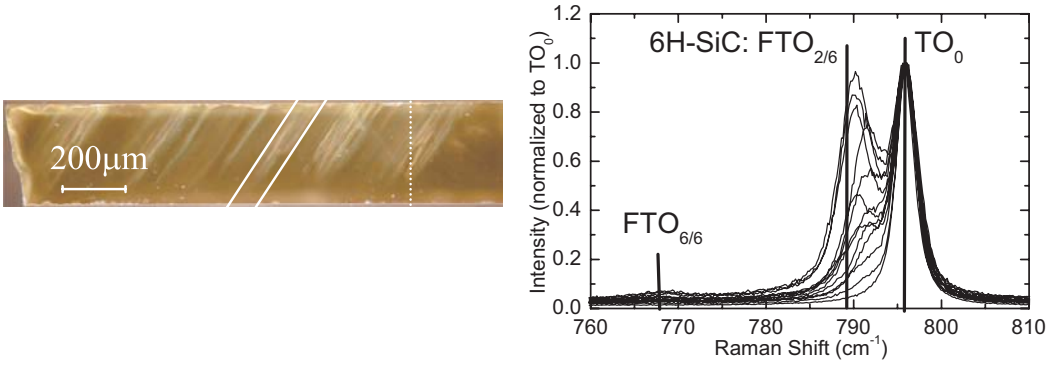

Figure 3 (online colour at: www.pss-b.com) Left: Darkfield microscopic image of the (110) cross section of the CVD sample annealed at 1700 °C. Right: Raman spectra taken along the dotted line shown in the microscope image. Vertical lines mark the frequencies of the TO modes of 6H-SiC.

planes of the 3C-SiC host crystal as indicated by the solid lines in Fig. 3. A series of Raman spectra taken along the dotted line spanning bright and dark regions of the crystal are shown on the right of Fig. 3. The distance between the measurement points was about 5 μm to 10 μm. In this graph, the expected frequency of the 6H-SiC $FTO_{2/6}$ mode is marked by a vertical line. It is evident that the frequency of the observed mode is shifted by 1 cm^{-1} to 5 cm^{-1} towards higher energies whereas the TO_0 mode remains fixed at the expected value of 796 cm^{-1}. The frequencies obtained by a line fit analysis are shown in Fig. 4. The frequency of the TO_0 mode and the frequency of the lower frequency mode are plotted as a function of the vertical position with 1 at the top of the micrograph. The frequency shift of the TO_0 mode is smaller than 0.5 cm^{-1}, whereas the frequency of the low lying mode is strongly dependent on the position on the sample. At no position do the intensity and frequency of this mode correspond to those of the reference 6H-SiC crystal $FTO_{2/6}$ mode. Furthermore, the line analysis shows that the lower frequency peak is broadened

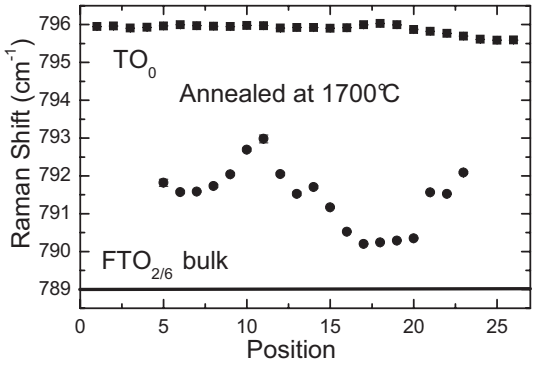

Figure 4 Frequency of the TO_0 mode (squares) and of the lower frequency mode (circles) as a function of the vertical position on the sample of Fig. 3. Position 1 is above and position 26 is below the translucent region along the dotted line in Fig. 3. The frequency of the 6H-SiC $FTO_{2/6}$ mode is indicated by the horizontal line. Note that for positions below 4 and above 23 the lower frequency mode was too weak in order to reliably give a value for its frequency.

by about a factor of two compared to the TO_0 phonon mode. This result is in clear contrast to the results obtained for annealing temperatures of 1800 °C and above, where the Raman spectra are concordant with the spectrum taken on a reference 6H-SiC sample. For the 1700 °C annealing temperature the polytype transformation to 6H-SiC is obviously still in its initial stage and therefore no clear polytype assignment can be made for the observed inclusions.

3.3 Crystal structure after PVT growth We now focus on crystal growth using the PVT-technique on CVD grown 3C-SiC seed crystals. Typical microscopic darkfield images of one PVT-sample grown at ~1900 °C are shown in Fig. 5. The left image (a) shows a (110) and the right (b) a $(\bar{1}10)$ cross section. On the (110) slice, areas of different colour are clearly visible in the grown crystal as well as in the seed crystal. This contrast can be assigned to polytype changes within the sample. Cubic 3C-SiC appears in different shades of yellow brown due to its small bandgap of 2.3 eV, whereas the 6H-SiC polytype with a low doping concentration has low absorption in the visible spectral range and appears white or grey in the darkfield micrographs of Fig. 5. Note that the region around position A in Fig. 5a is dark grey due to the dark background behind the sample. This inclusion is surrounded by yellowish 3C-SiC parts with boundaries indicated by the parallel white lines in the figure. There is another transparent inclusion slanted in opposite direction in the (110) cross section also marked with a white line in Fig. 5a. We measure an angle of 54.5° between the boundaries of the inclusions and the $[\bar{1}10]$ direction for both inclusions. This is in good agreement with the angle of 54.7° between the (111) and the (100) planes. Hence, the boundary lines are likely to be projections of the $(\bar{1}11)$ plane for the right inclusion and of the $(1\bar{1}1)$ plane for the left inclusion onto the surface of the (110) cross section, respectively. Raman spectra taken at different spots on the crystal (labelled A, B, and C in Fig. 5a) are shown in Fig. 6a.

The spectrum at position A is taken in a translucent region, that labelled C in a yellow region, and the spectrum labelled with B is taken in the seed 3C-SiC CVD layer, in

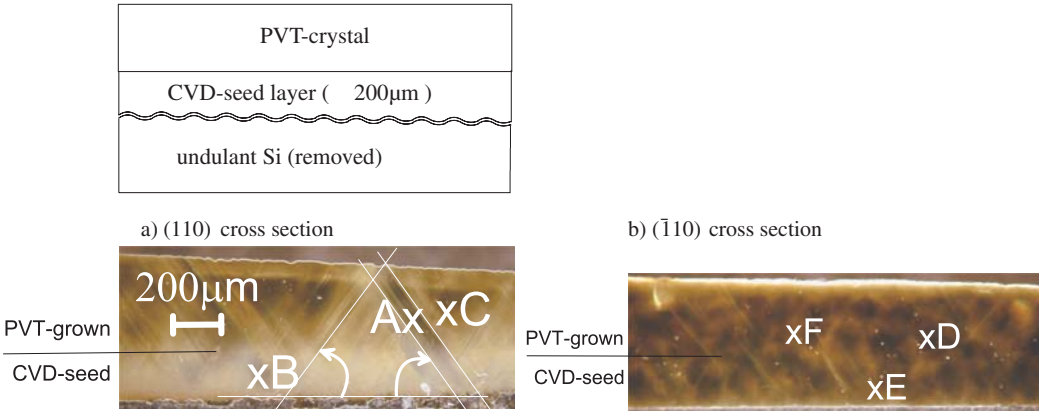

Figure 5 (online colour at: www.pss-b.com) Schematic of the samples investigated here and darkfield microscopic images of a) the (110) and b) the (1̄10) slice of crystal and seed grown at T_A = 1900 °C. Note the disappearance of the sharp colour contrasts when going from a) to b).

continuation of a translucent region in the grown crystal. The spectra clearly prove that the transparent regions A and B consist mainly of 6H-SiC, whereas the yellowish parts C consist exclusively of 3C-SiC. No other polytype inclusions are observed. Raman spectra taken in the seed crystal following a transparent region of the grown part (point B) prove that the seed crystal is also partly converted to 6H-SiC despite the fact that the CVD-layers were checked positive for 3C-SiC phase purity before growth. On the other hand, we confirm the 3C-SiC structure in the CVD seed layer below 3C-SiC domains (e.g. below C) in the PVT grown part.

We now turn to the slices that were cut at right angles to that of Fig. 5a such that the faces are parallel to the (1̄10) crystallographic planes of 3C-SiC. The optical micrograph of that cross section is shown in Fig. 5b and the appearance is of a grainy but rather uniform yellow brown colour. In particular, there is no optical evidence for 6H-SiC inclusions with well defined boundaries as they were observed on the (110) cross section.

However, the Raman spectra taken at the positions D, E, and F (see Fig. 6) give convincing evidence that the probed volume consists of a mixture of 3C-SiC and 6H-SiC with varying composition, where the contribution of 6H-SiC in spectrum D is of the order of 5%. From the comparison of the two cross sections with perpendicular orientation, we conclude that the sharp boundaries seen on the (110) oriented cross section are the projections of (1̄11) and (1 1̄1) crystallographic planes that run perpendicular to the (110) plane. Hence, when viewed from the perpendicular direction the 6H-SiC inclusions are stacked on top of each other such that the light crosses 6H- and 3C-SiC regions giving the uniform colour appearance observed in the micrograph of Fig. 5b.

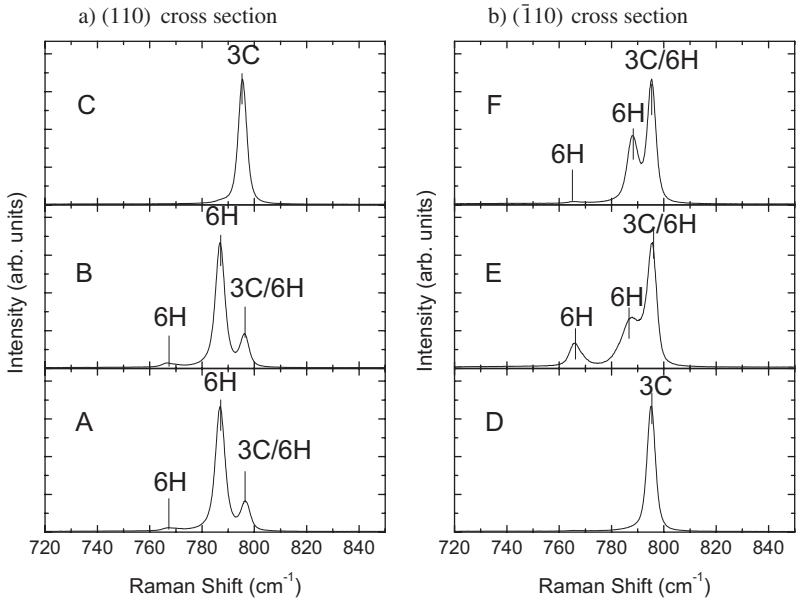

Figure 6 Raman spectra taken at positions A, B, and C on the (110) cross section (see Fig. 5a) and spectra taken at the positions D, E, and F on the (1̄10) cross section (see Fig. 5b).

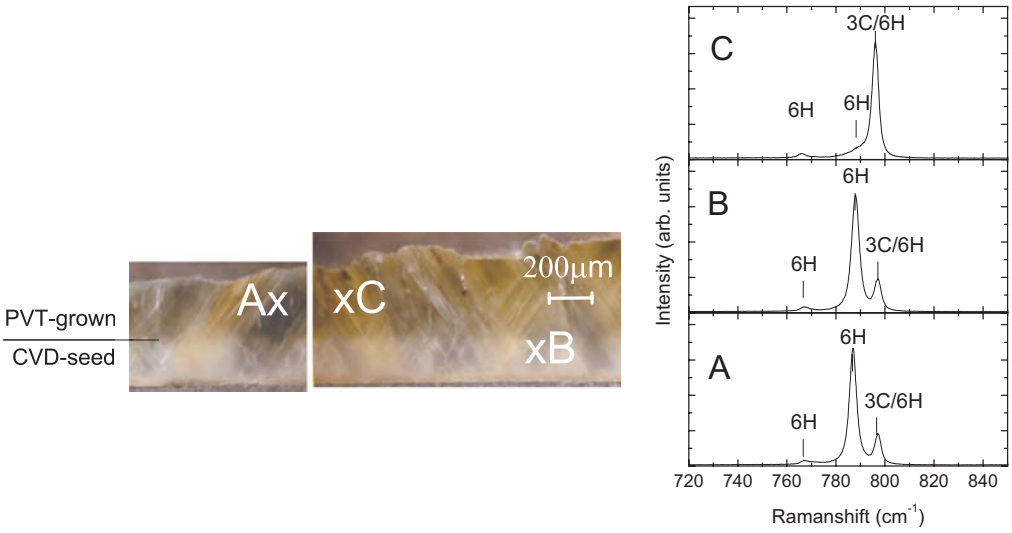

Figure 7 (online colour at: www.pss-b.com) Left: Darkfield microscopic images of an (110) cross section of a PVT crystal grown at 1930 °C. Right: Raman spectra taken at the positions indicated in the microscopic images.

The cross section parallel to (110) of a second 3C-SiC crystal grown at a temperature that was 30 K higher (~1930 °C) than the previous one is shown in Fig. 7a. Although the image shows features similar to those of the previous growth run (see Fig. 5a), the relative 6H-SiC fraction of the crystal is obviously larger at higher growth temperature. Although the contrast between the different polytype segments is not as clear as in the low temperature growth, the borders parallel to the $(\bar{1}11)$ and $(1\,\bar{1}1)$ planes are clearly observed.

Again, the Raman spectra taken at the positions A, B, and C (Fig. 7) prove that some parts of the grown crystal are purely 3C-SiC (C), whereas the transparent portions (A) are 6H-SiC. As for growth at 1900 °C, the 6H-SiC inclusions can be traced back to the CVD seed crystal (B), i.e. there is a correlation between the polytype at the growth interface and that of the grown crystal. We repeat, that both CVD seed crystals were purely 3C-SiC before commencing PVT growth.

3.4 Discussion of polytype conversion in 3C-SiC

The different polytypes of SiC can conceptually be visualised as evolving from the simple cubic (zinc-blende, 3C-SiC) or hexagonal (wurtzite, 2H-SiC) crystal structures by an ordered array of stacking faults along the [111] or *c*-direction. Since the formation energies of stacking faults in SiC are approaching zero or might even be negative at $T = 0$ [10] it comes as little surprise that for entropy reasons 3C- and 2H-SiC are the thermally least stable polytypes of SiC at finite temperature [11]. A detailed study of the temperature driven 3C → 6H polytype conversion has been presented by Yoo and Matsunami at finite temperatures [12]. They used ~300 μm thick, free-standing 3C-SiC crystals grown heteroepitaxially on unstructured Si(100) substrates by CVD that were annealed in argon for times comparable to the ones employed here. For temperatures above 21520 °C, a 3C → 6H polytype conversion was observed by photoluminescence and Raman spectroscopy that proceeded from the free (100) surfaces towards the center of the crystal slab with annealing time. Information about phase boundaries were not given. The results presented here for the CVD seed crystals also show a temperature driven 3C → 6H transformation but differs in essential details:

1. The phase transformation occurs at lower temperatures, namely at 1800 °C.

2. The phase transition proceeds from the free surface only towards the bottom and no phase transformation whatsoever is detected on the side that used to be the SiC/Si interface.

3. The 6H-SiC phase is confined to slabs that are sharply defined by $(1\,\bar{1}1)$ and $(\bar{1}11)$ crystallographic planes.

4. At the lowest annealing temperature (1700 °C) the Raman spectra indicate that the 3C → 6H phase transformation occurs via an intermediate stage that appears to be characterised by an incomplete rearrangement of *c*-planes towards the stacking sequence of 6H-SiC.

Since CVD growth, annealing treatment, and analysis were done under very similar conditions it is reasonable to try to trace the differences observed here to the special choice of substrate, namely "undulant Si". As elaborated in a series of publications by Nagasawa et al. [5–7] misfit dislocations are created at the Si–SiC interface in order to accommodate the large lattice mismatch between Si and 3C-SiC, and elastic deformations or incoherent grain boundaries exist at points where individual crystallites coalesce. These unstable deformations and defects are converted into fairly stable planar defects within a few μm of the interface as estimated from the micrographs in Ref. [5]. The planar defects consist of extended stacking faults one to three double layers thick with general {111} orientation of their coherent boundaries. This yields two pairs of twin

boundaries: One pair parallel to (111) and $(\bar{1}\,\bar{1}\,1)$ and hence a lateral orientation parallel to the groves on the undulant Si substrate and another pair parallel to the $(1\,\bar{1}\,1)$ and $(\bar{1}11)$ crystallographic planes that are oriented essentially perpendicular to the groves. The "parallel" set disappeares in the course of CVD growth whereas at the same time the "perpendicular" set extends laterally. Since either a pair of $(1\,\bar{1}\,1)$ planes or a pair $(\bar{1}11)$ planes delimitate the 6H inclusions in our samples, it is suggestive to assume that these planes correspond to the stacking faults that are the dominant and characteristic defects in 3C-SiC CVD crystals grown on undulant Si [5]. These stacking faults are natural starting points for a phase transition that comprises an ordered array of stacking faults.

The polytype conversion does not proceed down to the original Si–SiC interface and we argue that this is due to the existence of twin boundaries parallel to (111) and $(\bar{1}\,\bar{1}\,1)$ planes that cross the domains already converted to 6H-SiC.

We note that there is no signature of polytypes other than 3C- and 6H-SiC above 1800 °C and the Raman spectra resemble those of the respective bulk crystals. However, at the lowest annealing temperature (1700 °C) the frequencies of the observed phonon modes greatly deviate from those known for 6H-SiC as discussed above. We conclude that at the low annealing temperature there is only an incomplete rearrangement of *c*-planes that is completed for annealing temperatures at and above 1800 °C.

4 Electronic Raman studies of shallow donors in silicon carbide Application of silicon carbide in devices requires low resistivities of the n-type doped material, i.e. a high concentration of electrically active shallow donors. In order to obtain a high donor concentration, co-doping with phosphorus (P) in addition to the conventional nitrogen (N) donor has recently been considered as an alternative because P is expected to occupy Si-sites whereas N occupies C-sites [13]. Raman spectroscopy has been used in the past for the characterization of N-doped SiC and the existence of electrically active donors has been directly deduced from Raman transitions of electrons between the respective donor ground state and its valley-orbit-split excited state. For the case of phonon Raman scattering discussed in the previous section a phonon, i.e. a vibrational excitation of the crystal lattice, is generated during the scattering process. In the electronic Raman scattering process discussed in this section the vibrational state remains unchanged, but an electronic excitation is generated. This section deals with the excitations of electrons from the ground state to an excited state at the same donor site. The energy of the scattered light that is detected in the same principle experimental setup as for phonon Raman scattering allows to determine the energy required for the electronic excitation from the Raman shift. From electronic Raman spectra one thus can differentiate between donors of different excitation energies. Electronic Raman scattering does, however, not allow to access the ionization energy of the respective donor states directly from the Raman shift since the donor electron is not excited to the conduction band edge. The excitations that we deal with in this section are transitions of the electrons between the valley orbit split 1s-ground states of the shallow donors. Different valley orbit energies are expected for donors occupying inequivalent lattice sites in the SiC crystals. For N-doped SiC, a series of valley orbit splittings observed in low temperature Raman spectra has been attributed to the different lattice sites of the corresponding donor [14, 15]. As an example, 6H-SiC has three different sites on the carbon sublattices – two cubic and one hexagonal site. However, for the N-donor more electronic Raman signals were found not only for 6H-SiC, but also for 4H- and 15R-SiC. Here we study different polytypes of SiC co-doped with P and N and present Raman spectra that can be attributed unambiguously to the valley orbit transitions of P.

4.1 Experiments These experiments require the samples under investigation to be cooled to temperatures that can be accessed only using liquid helium. Hence, the samples were mounted in a He-cryostat so that the temperature could be adjusted in the range of $7\ \mathrm{K} < T < 300\ \mathrm{K}$. We reduced the laser power to below 35 mW in order to reduce the heating during experiments. Some of the electronic Raman signals have low excitation energy and are consequently spectrally very close to the laser line, requiring high spectral resolution. The highest resolution could be obtained with the longer wavelength line from a HeNe-laser (633 nm). Also, before directing the laser light on the samples, it was spectrally filtered in order to remove contributions of light that are spectrally close to the laser line.

4.2 Samples Two sets of samples were investigated here. One sample set consisting of 6H-, 4H-, and 15R-SiC polytypes was doped during bulk growth in a modified physical vapor transport (MPVT) reactor employing a gaseous PH_3-source that was directly fed into the reactor for P doping [16, 17]. The PH_3-flow was varied during growth in order to obtain SiC-samples with varying P concentration as well as a reference sample without P. The successful incorporation of P was checked using Time-of-Flight secondary ion mass spectroscopy (TOFSIMS). A maximum concentration of phosphorus of $1.5 \times 10^{18}\ \mathrm{cm}^{-3}$ was determined. These samples were co-doped with nitrogen at a concentration of $2 \times 10^{18}\ \mathrm{cm}^{-3}$.

An alternative set of samples was doped with phosphorus using the neutron transmutation doping (NTD) technique [18]. In this technique the nuclear reaction of the ^{30}Si isotope after capture of thermal neutrons to ^{31}P was applied for doping. The samples were annealed after transmutation at 1700 °C. In order to achieve a sufficiently high doping concentration the samples for this experiment were grown with isotopically enriched Si-source material (50% of ^{30}Si). In this way, the P-concentration is more than ten times larger than what is possible for SiC with a natural isotopic composition (3.1% ^{30}Si). The samples doped by NTD con-

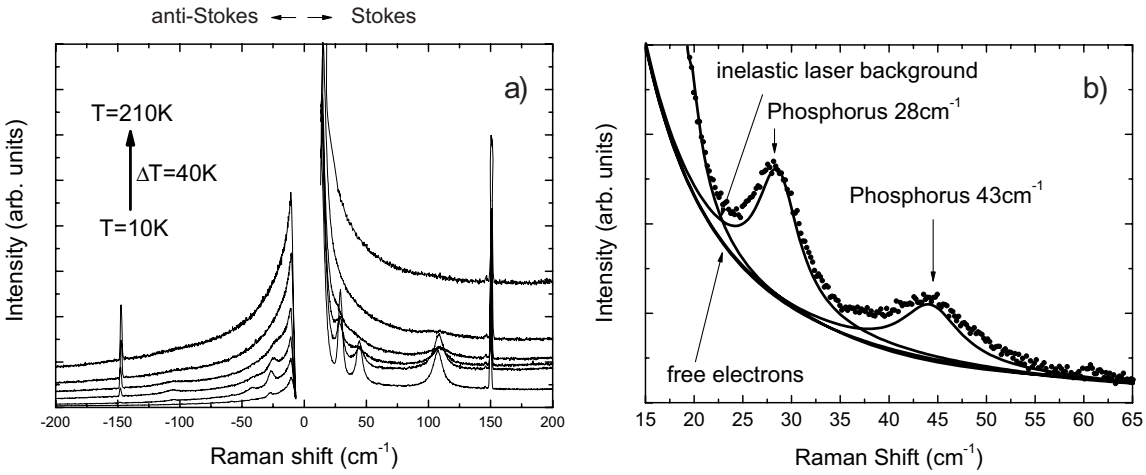

Figure 8 a) Low energy Raman spectra of P and N co-doped 6H-SiC recorded on both sides of the laser lines and for different temperatures. b) Low-energy Stokes section of the Raman spectrum at 70 K (filled dots) fitted by the superposition of energy-dependent excitations of free electrons, a background of inelastically scattered laser light, and two peaks at 28 cm^{-1} and 43 cm^{-1}, which we assign to electronic transitions between the valley orbit split 1s states of P donors on different lattice sites.

tained about 2×10^{18} cm^{-3} phosphorus and we did detect only little electrically active nitrogen donors (N-concentration below 5×10^{16} cm^{-3}). We had available 6H- and 15R-SiC polytypes doped by the NTD-technique for our measurements.

4.3 Results As an example, we show in Fig. 8a a series of Raman spectra of a 6H-SiC sample that is co-doped with N and P (nitrogen: 2×10^{18} cm^{-3}, phosphorus: 1×10^{18} cm^{-3}) recorded at temperatures between 10 K and 210 K. In these spectra which cover the Stokes and anti-Stokes low energy part of the spectrum a series of peaks appears, which are due to electronic transitions as well as signals due to phonon scattering at ± 150 cm^{-1}. The peaks are superimposed on a broad background that increases towards the laser line. The background increases with temperature and is asymmetrical, i.e. larger for Stokes than for anti-Stokes scattering. We assign this background to electronic Raman scattering by the collective excitation of free electrons [19]. The temperature dependence of the free-electron background reflects the thermal excitation of electrons from the donors to the conduction band. The electronic signals, which show up as peaks in Fig. 8a at about 30 cm^{-1}, 40 cm^{-1}, and 110 cm^{-1}, have the opposite trend. They are visible at low temperature and tend to disappear at higher temperatures. They are consequently assigned to Raman transitions between the localized states of shallow donor impurities. Hence, their disappearance at high tem-

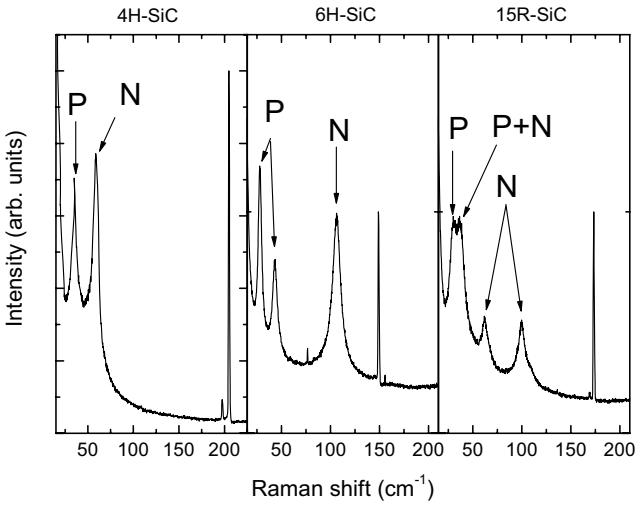

Polytype	N Energy (meV)	P Energy (meV)
4H	7.3	4.3
	4-5 Peaks: 65.5-78.3	2.2
6H	13	3.5
	60.5	5.3
	62.6	
	77.9	
	78.9	
15R	4.7	3.5
	7.4	4.3
	12.1	
	3-4 Peaks: 50.8-56.5	

Figure 9 Raman spectra of SiC-polytypes co-doped with N and P taken at 10 K. We assign the peaks marked by arrows to electronic excitations between the valley–orbit split 1s ground state levels of the shallow donors N and P. The sharp peaks above 150 cm^{-1} are due to Raman scattering of the folded TA-phonon modes. The table lists the energies of all valley orbit splittings, which we have measured for the N and P donors.

perature reflects the ionization of the donor state, i.e. the thermal excitation of its electron to the conduction band.

In order to quantify the contributions of electronic Raman signals from shallow donors we fitted each Raman spectrum to the sum of two Lorentzians, the contribution of scattering from free electrons according to Ref. [19] and a background of inelastically scattered laser light as shown in Fig. 8b.

By analyzing and comparing N-, P-, and co-doped samples, we could assign each peak observed in the spectra of polytypes investigated here to either P or N donors. The results of this assignment for the co-doped samples are summarized in Fig. 9. The numbers of N-related peaks and their energies are in agreement with results reported in the literature [15].

4.3.1 Symmetries of Raman transitions All polytypes of SiC are indirect semiconductors. As a result of the crystal symmetry, there is more than one conduction band minimum in the Brillouin-zone. In the case of 6H-SiC these are six minima located on the M–L lines of the Brillouin zone. In the effective mass approximation, the localized donor wave functions are expanded in terms of Bloch functions of the respective conduction band minima which are combined to form symmetry-adapted linear combinations of Bloch sums. Although the wave functions describing the different conduction band minima are degenerate, the possible linear combinations yield donor states that split into states with different energy. The 1s ground state, as a result, is split into two different levels. The valley orbit transitions that we observe here, are transitions induced between these 1s states. In order to determine the symmetry of these valley orbit transitions and hence that of the states involved, we recorded polarized Raman spectra from *a*-plane cross sections, i.e. ones where the *c*-axis lies in the plane of the sample. For the case of the *a*-plane 6H-SiC shown in Fig. 10, all three signals are observed only in the *x*(*yy*)-*x* geometry, i.e. when the incident and detected light are both polarized perpendicular to the *c*-axis. The Raman-allowed symmetries of the transitions as obtained from group theory, are given in the figure for each particular scattering geometry. In addition we have also considered two possible symmetries for the donor; C_{3v} corresponds to the local symmetry of the donor atom, whereas C_{6v} is the symmetry of the crystal. The result that the signals are only observed in *x*(*yy*)-*x* geometry proves that the transition has the E_2 symmetry of C_{6v}. This further implies that the states involved as initial and final states in this transition have E_2 and A_1 symmetries, but there is no possibility to distinguish between the symmetry of the ground and the valley orbit split excited state. We derive the same symmetry assignments for the hexagonal 4H-SiC polytype as well, whereas the symmetry of transitions in 15R-SiC have the E symmetry of C_{3v}.

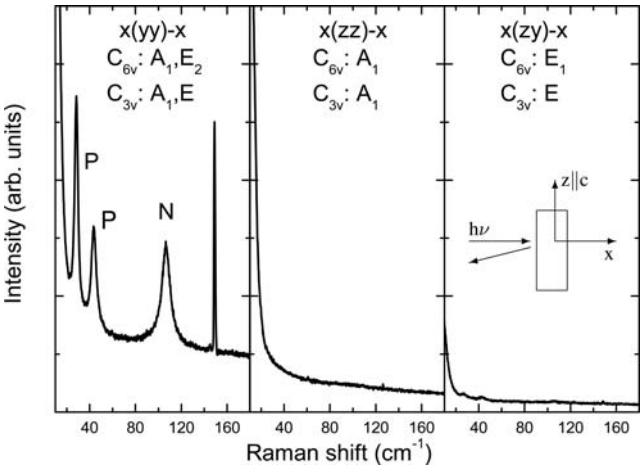

Figure 10 Raman spectra of 6H-SiC measured on the *a*-plane with different scattering geometries. The notation for the scattering geometry is given in the top of the figures, where the first and last letter denote the direction of incident laser light and scattered light, respectively. The letters given in brackets are the polarization of incident and detected light, respectively. The coordinate system is chosen as shown so that *x*-axis is perpendicular to the surface, whereas the *z*-axis is along the crystal *c*-axis. The valley–orbit transitions are observed only in *x*(*yy*)-*x* geometry, i.e. when the polarization vectors of the impinging and scattered light are both perpendicular to the *c*-axis of the crystal.

4.3.2 Temperature dependence of Raman intensities and defect occupation The disappearance of the electronic Raman signals with increasing temperature (see Fig. 8a) reflects the thermal excitation of electrons from the donor ground state to the conduction band. In this section we track the degree of donor ionization as a function of temperature by measuring the temperature dependence of Stokes and anti-Stokes intensities and deriving the occupation of the 1s-ground state therefrom. To that end we normalized the Raman intensities as obtained from the line fit analysis to the phonon scattering intensities, taking the phonon peak intensities according to Bose statistics into account. The Stokes- and anti-Stokes-intensities so obtained are given in Fig. 11 as open circles, respectively, where Stokes intensities are generally larger than the anti-Stokes intensities. From these intensities the total occupation of the valley orbit split 1s-states is calculated as a weighted sum, where the weighting factor for the Stokes-signal is given by the ratios of degeneracy-factors g of the two states involved. We assumed $g = 4$ for the ground state and $g = 8$ for the valley orbit split state [20]. In the left graph of this figure, the results for the two Raman signals assigned to P are shown, whereas the right graph gives the results for three signals assigned to N. The corresponding Raman shift is given in each figure. The ionization, i.e. the reduction of occupation, is governed by the ionization energies of the respective donor levels. What we can infer for 6H-SiC from the results of Fig. 11 is, that the two electronic states of phosphorus [28 cm^{-1} (3.4 meV) and 43 cm^{-1} (5.3 meV)] and the nitrogen related state with 108 cm^{-1} (13 meV) are relatively shallow since their occupation is reduced to one half at about 100 K. The remaining nitro-

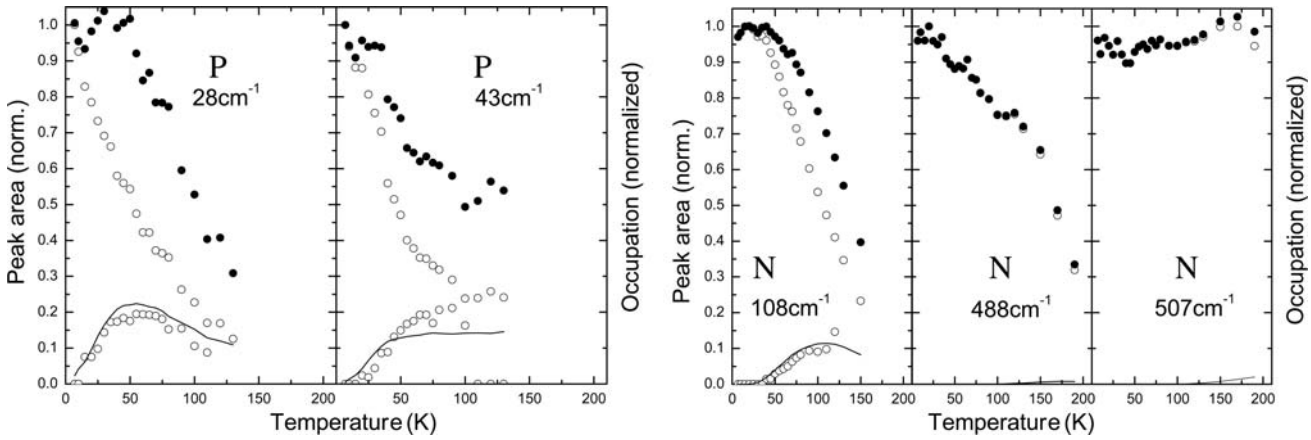

Figure 11 Left graph: Normalized Raman intensities (open circles) of Stokes and anti-Stokes scattering signals in 6H-SiC for P-related electronic Raman peaks as a function of temperature. The solid line corresponds to the anti-Stokes intensity calculated with the Stokes intensity and a Boltzmann-factor with the valley orbit splitting as the activation energy. Filled circles show the total occupation of the respective 1s-levels normalized to their maximum value for $T = 4$ K. Right graph: Same for N-related defects.

gen-related signals are observed at temperatures as high as 200 K. Hence, the transitions at 488 cm^{-1} and 507 cm^{-1} (60.5 meV and 62.6 meV) belong to N-related defects with ground states that lie considerably deeper in the gap.

4.4 Conclusions The Raman scattering signals in P-doped SiC consist as in the case of N doping [14, 15] of a series of polytype-dependent signals which are attributed to the lattice site-dependent valley orbit splitting of the 1s donor ground state. In contrast to the N donor, all peaks have frequencies below 43 cm^{-1} or 5.3 meV. We carefully checked the range of energies between 10 cm^{-1} and 2000 cm^{-1} and did not observe any other significant electronic Raman signals except those listed in the table of Fig. 9. In agreement with previous work on N-doped SiC [15], the number of N-related electronic Raman signals exceeds the number of inequivalent lattice sites of the carbon-sublattice (e.g. 5–6 peaks in 4H-SiC vs. 2 inequivalent sites). Also, many of the N-related signals have energies above 60 meV, a factor of 10 larger than the highest energy observed for P. Therefore we tend to ascribe all signals below 110 cm^{-1} (14 meV) to the valley orbit splitting of both P and N, whereas the additional high energy N-related signals might consequently be due to other than substitutional configurations.

All P-related peaks in the Raman spectrum as well as the low energy N-related peaks decrease in intensity with increasing temperature. This behavior is explained by the thermal excitation of the donor bound electrons to the conduction band. Generally, the Raman peak intensity decreases to less than half of its value at $T = 7$ K at around 100 K. This is different for the high energy peaks of N-doped samples, some of which persist unattenuated up to 200 K. Hence, we believe that these signals might be related to deep, as yet unassigned N-related defects rather than to shallow donor states.

5 Graphene layers on SiC-surfaces At temperatures above 1200 °C silicon starts to evaporate from the SiC-surface leaving behind an excess of carbon. By careful control of the process parameters it is possible to obtain a monolayer of carbon on the surface that is epitaxially oriented with respect to the substrate in the form of a two dimensional graphene lattice [21, 22]. Graphene, a single sheet of carbon atoms isolated as it were from graphite, is a zero gap semiconductor, constitutes the ultimate two dimensional electron system, and exhibits a linear dispersion relationship near the Fermi energy such that the low-lying excitations behave like massless relativistic Dirac fermions [23]. On account of these unusual properties it has outstanding electronic transport properties that qualify it as an emergent electronic material [24]. Research on graphene has utilized so far predominantly graphene flakes that were obtained by exfoliating graphite [25] and Raman spectroscopy has been shown to offer a means to differentiate between different numbers of graphene layers [25]. In this section we employ Raman spectroscopy to analyze the structure of few layer graphene grown thermally on the Si-terminated 6H-SiC(0001) surface.

5.1 Synthesis and Raman experiments of graphene In order to synthesize few layer graphene (FLG), n-type 6H-SiC(0001) was annealed at temperatures above 1200 °C and the area averaged thickness of the resulting graphene film was determined by X-ray photoelectron spectroscopy utilizing the attenuation of the substrate signal by the overlayer [26]. Different samples were studied: Samples with a nominal thickness of 1.5 layers and 6 layers, respectively, a highly oriented pyrolytic graphite (HOPG) sample, and a reference SiC-sample without graphitization. In the following we concentrate on two prominent features in the Raman spectrum of graphite: The zone centre LO-phonon around 1580 cm^{-1} (G-peak) and the two-phonon peak around 2700 cm^{-1} which corresponds to

the doubly resonant excitation of two phonons close to the K-point in the Brillouin zone of graphene (2D-peak). Whereas the detection of the 2D-line is possible without any significant interference from the SiC substrate, the intensity of the G-peak of FLG is much weaker than the two-phonon spectrum of the underlying SiC-substrate. Hence, accumulation times in the order of 10 min are necessary in order to achieve a statistical accuracy of the spectra high enough to correct the G-spectrum of FLG for the SiC contribution.

5.2 Results Figure 12 shows Raman spectra of a nominally 1.5 layer graphene sample in the region of the 2D-peak. Here no interference from the SiC substrate is encountered as demonstrated by the bottom spectrum of Fig. 12 and the spectra are solely due to the graphene overlayer. Depending on the position on the sample, a single Lorentzian line at 2744 cm^{-1} is observed or a considerably broader one centred at about 2724 cm^{-1}. The latter has been successfully deconvoluted into four components as indicated in Fig. 12 by the solid lines. Drawing from the work of Graf et al. [25] on exfoliated graphene, we associate the single line with a monolayer of graphene and the component line with a bilayer. Hence, as expected, the nominal 1.5 graphene layer consists of a mixture of 1 and 2 layers of graphene, distributed statistically over the SiC surface. While the line shapes of each spectrum agree with those measured on exfoliated graphene their positions do not. Whereas Graf et al. report line positions of the G-peak essentially in agreement with HOPG we measure a significant blue shift that depends moreover on the number of graphene layers as demonstrated in Fig. 13, in which we show the Raman spectra of the G- and 2D-peaks recorded on samples with different thicknesses of FLG. In comparison to HOPG, both G- (Fig. 13a) and 2D-peak (Fig. 13b) are shifted to higher frequencies with the maximum shift measured for the graphene monolayer. At some positions of the sample we record Raman spectra that are composed of

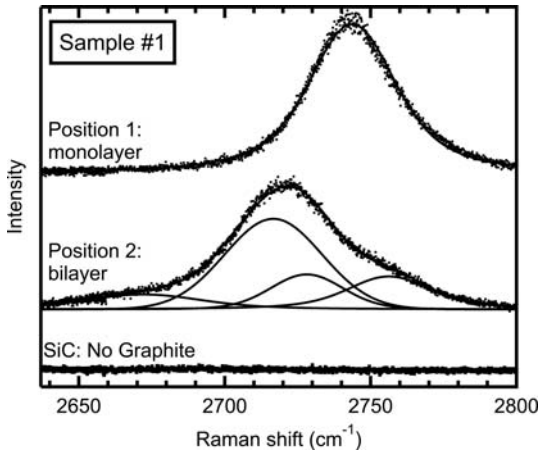

Figure 12 Raman spectra taken at different spots on a FLG sample (#1) with an average thickness of 1.5 graphene layers, and the Raman spectrum of a reference spectrum of pure SiC. One spectrum (position 1) has a single component, whereas the second spectrum (position 2) consists of four components and is shifted towards lower frequency.

two components in the G-peak region as shown in Fig. 13a (spectrum labelled mono- and bilayer). Obviously, in this region the sample is inhomogeneous on the scale of the laser spot (2 μm) and consists of a mixture of mono- and bilayer domains. The frequencies of the G-peaks and the centre of mass of the 2D-peak spectra are plotted versus the number of layers in Fig. 14a and b, respectively. The maximum phonon hardening with respect to HOPG occurs for monolayer graphene and amounts to 30 cm^{-1} and 38 cm^{-1} for the G- and 2D-peak, respectively.

5.3 Discussion The phonon lines that we observe for FLG are significantly shifted to higher frequencies compared to HOPG and exfoliated graphene layers [25]. The phonon-frequency shift is particularly large for the graphene monolayer. For the phonon hardening of the epi-

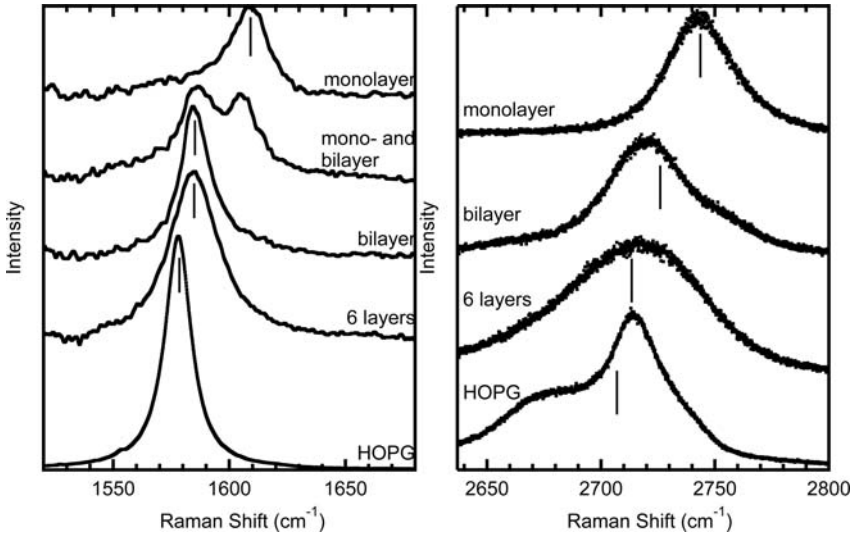

Figure 13 Raman spectra of the G- (left) and 2D-lines (right) of HOPG and few-layer graphene on 6H-SiC. For the G-lines of the FLG-samples the spectra were obtained by subtracting the Raman spectrum of bare SiC. The vertical tick marks indicate centers of gravity of the lines as they are gathered in Fig. 14.

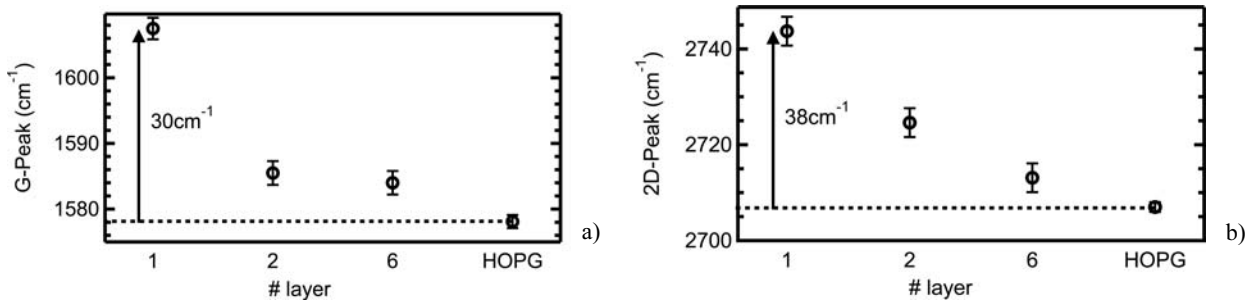

Figure 14 Frequency of the G-peak (a) and of the centre of mass frequency of the 2D-peak (b) as a function of the number of graphene layers. The respective frequencies for bulk graphite (HOPG) are marked by broken lines.

taxial monolayer on the $\left(6\sqrt{3}\times 6\sqrt{3}\right)$ reconstructed SiC surface we consider two alternatives: a reduction of the effect of the Kohn-anomaly or compressive strain induced in the graphene layer by the underlying substrate. The Kohn anomaly leads to a softening of the LO-branch at the Γ-point of the Brillouin-zone for uncharged graphene [27]. Since the graphene monolayer on the SiC surface is negatively charged [28], a reduction of the Kohn anomaly induced phonon softening could explain the observed frequency shift of the G-peak. However, a frequency shift of the 2D-peak would not be expected by the same mechanism [29]. Hence, we exclude a reduced Kohn-anomaly as the main cause for the observed frequency shift.

Compressive strain transferred from the substrate to the graphene overlayer, on the other hand, would affect the entire phonon dispersion curves and hence would result in an upshift of the G-peak as well as the 2D-peak. In order to estimate the influence of strain we assume that graphene is free of stress at the formation temperature. With the thermal expansion coefficient of SiC [30] we calculate a relative reduction of the lattice constant of $\Delta a/a = -9\times 10^{-3}$ when cooling the sample from the graphene formation temperature down to room temperature. Bulk graphite, on the other hand, has a smaller expansion coefficient for the in-plane lattice parameter and the relative change in in-plane lattice constant $\Delta a/a = -1\times 10^{-3}$ over the same temperature range [31]. Since the SiC substrate is much thicker than the graphene monolayer the ensuing strain will be taken up entirely by the graphene overlayer if no relaxation takes place during cool down. Hence, compared to a free standing graphene layer, a maximum strain of $\Delta a/a = -8\times 10^{-3}$ in the epitaxial layer is to be expected. From the strain coefficient of the zone-centre phonon frequency of graphite given in Ref. [32] we calculate a strain-induced upshift of the G-line by 45 cm^{-1}. Since this value is larger than the observed shift of 30 cm^{-1} it is reasonable to assume that some relaxation of the monolayer has occurred during cooldown.

5.4 Conclusion We demonstrate here that Micro-Raman spectroscopy is sensitive enough to measure Raman spectra of FLG down to the monolayer level even in the presence of strong interfering lines from the SiC substrate. Moreover, we are able to distinguish mono- from bilayer graphene and from graphene layers with a higher number of layers on the basis of their Raman line shapes. An additional distinguishing feature is a Raman line shift that depends on the number of graphene layers and is strongest for monolayer graphene. Since this phonon hardening is not observed in exfoliated graphene layers, we suggest that it is the result of compressive strain that builds up during cooldown of the sample from the graphene formation temperature due to the different thermal expansion coefficients of graphite and SiC.

6 Summary In this paper we present three case studies for the application of Raman spectroscopy to material science aspects of SiC. They are the polytype conversion of 3C-SiC during high temperature annealing, the study of SiC co-doped with nitrogen and phosphorus, and epitaxial graphene layers on SiC surfaces produced by vacuum annealing.

We find that 3C-SiC grown with a special CVD technique on silicon [5] partially converts to 6H-SiC at annealing temperatures of 1800 °C and higher. Polytype conversion already sets in at 1700 °C; however, at that temperature the material is dominated by stacking disorder giving Raman spectra that strongly deviate from the spectra of 6H-SiC. Successful bulk growth on CVD grown 3C-SiC is verified on those domains in the 3C-SiC substrate that are not converted to the hexagonal polytype.

We apply Raman spectroscopy to investigate various co-doped SiC-polytypes. We find a series of low frequency electronic Raman signals that we ascribe to electronic transitions at localized donor related sites. We assign all of the observed transitions with frequencies below 105 cm^{-1} to transitions between the valley orbit split donor ground states of donor atoms occupying inequivalent lattice sites. In contrast to phosphorus, there are additional higher energy transitions for nitrogen with Raman signals above 400 cm^{-1} (50 meV). We assign these peaks to electronic transitions at deep, N-related defects rather than to the valley orbit splitting of shallow donors on the basis of their temperature dependence.

We demonstrate that Raman spectroscopy is sensitive enough to observe few layer graphene at the SiC-surface.

From the shape of the Raman spectra we are able to distinguish mono-layers from double- or even higher number of layers of graphene. For a single graphene layer we observe considerable phonon hardening that we ascribe mainly to mechanical strain that builds up when the sample is cooled down to room temperature after its formation at elevated temperatures.

Acknowledgements We thank Th. Seyller, K. Emtsev, G. Pensl, K. Semmelroth, F. Schmidt, D. Wellmann, P. Desperrier, E. Haller, J. W. Ager, U. Starke, and H. Nagasawa for support. This work was supported by the German Science Foundation in the framework of SiC-Forschergruppe FOR 476 (project HU434/5-3).

References

[1] W. E. Nelson, F. A. Halden, and A. Rosengreen, J. Appl. Phys. **37**, 333 (1966).
[2] D. K. Ferry, Phys. Rev. B **12**, 2361 (1975).
[3] Y. Okui, C. Jacob, S. Oshima, and S. Nishino, Mater. Sci. Forum **389–393**, 331 (2002).
[4] A. Bakin, I. Behrens, A. Ivanov, E. Peiner, D. Piester, H.-H. Wehmann, and A. Schlachetzki, Mater. Sci. Forum **389–393**, 327 (2002).
[5] H. Nagasawa, T. Kawahara, and K. Yagi, Mater. Sci. Forum **389–393**, 319 (2002).
[6] H. Nagasawa, K. Yagi, T. Kawahara, and N. Hatta, Mater. Sci. Forum **433–436**, 3 (2003).
[7] N. Hatta, K. Yagi, T. Kawahara, and H. Nagasawa, Mater. Sci. Forum **433–436**, 273 (2003).
[8] K. Semmelroth, M. Krieger, G. Pensl, H. Nagasawa, R. Püsche, M. Hundhausen, L. Ley, M. Nerding, and H. P. Strunk, Mater. Sci. Forum **457–460**, 151 (2004).
[9] D. W. Feldmann, J. H. Parker, W. J. Choyke, and L. Patrick, Phys. Rev. **173**, 787 (1968).
[10] P. Käckell, J. Furthmüller, and F. Bechstedt, Phys. Rev. B **58**, 1326 (1998).
[11] G. A. Bootsma, W. F. Kippenberg, and G. Verspui, J. Cryst. Growth **8**, 341 (1971).
[12] W. S. Yoo and H. Matsunami, Jpn. J. Appl. Phys. **30**, 545 (1991).
[13] K. Semmelroth, F. Schmid, D. Karg, G. Pensl, M. Maier, S. Greulich-Weber, and J.-M. Spaeth, Mater. Sci. Forum **433–436**, 63 (2003).
[14] J. Colwell and M. V. Klein, Phys. Rev. B **6**, 498 (1972).
[15] S. Nakashima and H. Harima, phys. stat. sol. (a) **162**, 39 (1997).
[16] T. L. Straubinger, P. J. Wellmann, and A. Winnacker, Mater. Sci. Forum **353–356**, 33 (2001).
[17] See also the contribution by Wellmann et. al in this volume.
[18] H. Heissenstein, C. Peppermueller, and R. Helbig, J. Appl. Phys. **83**, 7542 (1998).
[19] G. Contreras, A. K. Sood, and M. Cardona, Phys. Rev. B **32**, 924 (1985).
[20] S. Greulich-Weber, phys. stat. sol. (b) **210**, 415 (1998).
[21] Th. Seyller, K. V. Emtsev, F. Speck, K.-Y. Gao, and L. Ley, Mater. Sci. Forum **556/557**, 701 (2007).
[22] See also the contribution by Th. Seyller et al. in this issue, phys stat. sol. (b) **DOI** 10.1002/pssb.200844143.
[23] K. S. Novoselov, A. K. Geim, S. V. Morozov, D. Jiang, Y. Zhang, S. V. Dubonos, I. V. Grigorieva, and A. A. Firsov, Science **306**, 666 (2004).
[24] C. Berger, Z. M. Song, X. B. Li, X. S. Wu, N. Brown, C. Naud, D. Mayou, T. B. Li, J. Hass, A. N. Marchenkov, E. H. Conrad, P. N. First, and W. A. de Heer, Science **312**, 1191 (2006).
[25] D. Graf, F. Molitor, K. Ensslin, C. Stampfer, A. Jungen, C. Hierold, and L. Wirtz, Nano Lett. **7**, 238 (2007).
[26] K. V. Emtsev, Th. Seyller, F. Speck, L. Ley, P. Stojanov, J. D. Riley, and R. G. C. Leckey, Mater. Sci. Forum **556/557**, 525 (2007).
[27] M. Mohr, J. Maultzsch, E. Dobardzic, S. Reich, I. Miloševic, M. Damnjanovic, A. Bosak, M. Krisch, and C. Thomsen, Phys. Rev. B **76**, 035439 (2007).
[28] T. Ohta, A. Bostwick, J. L. McChesney, Th. Seyller, K. Horn, and E. Rotenberg, Phys. Rev. Lett. **98**, 206802 (2007).
[29] A. Das, S. Pisana, S. Piscanec, B. Chakraborty, S. K. Saha, U. V. Waghmare, R. Yiang, H. R. Krishnamurhthy, A. K. Geim, A. C. Ferrari, and A. K. Sood, cond-mat.mtrl-sci (2007), arXiv:07091174vl.
[30] H. P. Liaw and R. F. Davis, J. Electrochem. Soc. **131**, 3014 (1984).
[31] D. K. L. Tsang, B. J. Marsden, S. L. Fok, and G. Hall, Carbon **43**, 2902 (2005).
[32] M. Hanfland, H. Beister, and K. Syassen, Phys. Rev. B **39**, 12598 (1989).